# Atomic level control of association-dissociation behavior of In impurities in polycrystalline ZnO

W. Sato,[1,2,*] M. Takata,[2] H. Shimizu,[2] S. Komatsuda,[3] Y. Yoshida,[4] A. Moriyama,[4] K. Shimamura,[5] and Y. Ohkubo[6]

[1]*Institute of Science and Engineering, Kanazawa University, Kanazawa, Ishikawa 920-1192, Japan*
[2]*Graduate School of Natural Science and Technology, Kanazawa University, Kanazawa, Ishikawa 920-1192, Japan*
[3]*Institute of Human and Social Sciences, Kanazawa University, Kanazawa, Ishikawa 920-1192, Japan*
[4]*Department of Physics, Kanazawa University, Kanazawa, Ishikawa 920-1192, Japan*
[5]*Engineering and Technology Department, Kanazawa University, Kanazawa, Ishikawa 920-1192, Japan*
[6]*Institute for Integrated Radiation and Nuclear Science, Kyoto University, Kumatori, Osaka 590-0494, Japan*

(Received 20 November 2021; revised 9 April 2022; accepted 18 May 2022; published 1 June 2022)

In the present work, we have succeeded in controlling association-dissociation process of thermally activated In impurities introduced in polycrystalline ZnO by a multistep doping method. The thermal behavior and eventual residential sites of In ions were monitored on an atomic scale by means of time-differential perturbed angular correlation spectroscopy with the $^{111}$In($\rightarrow^{111}$Cd) probe. The present doping method of combined heat treatments in air and in vacuum enabled the introduction of a great fraction of 0.5 at. % In donors into defect-free substitutional Zn sites. It was demonstrated that the In-containing ZnO samples show a clear positive correlation between the electrical conductivity and the concentration of In donors at substitutional Zn sites, achieving a conductivity as high as five orders of magnitude compared with undoped ZnO.

DOI: 10.1103/PhysRevMaterials.6.063801

## I. INTRODUCTION

Among various materials receiving high expectations for future applications, zinc oxide (ZnO) is one of the most promising compounds for next-generation electronic and spintronic materials and devices such as varistors [1,2], dilute magnetic semiconductors [3–6], transparent electrodes [7,8], and photocatalysts [9–11]. Especially, its application as substitutes for rare-metal oxides has been drawing attention reflecting the relatively abundant resource of Zn, and improvement of its electric property is becoming an urgent issue. As regards the semiconductor property, ZnO is known to exhibit intrinsic *n*-type conduction originating from defects inherent in the lattice such as O vacancies, interstitial Zn, and impurities like hydrogens inevitably involved in its synthesis processes. In addition to the intrinsic nature, it is known that doping with donor ions of group 13 elements (Al, Ga, and In) controls the semiconductor property of ZnO [12–14]. In order to maximize the potential of the donors, the search for the optimum amount of dopants and identification of their physical and chemical states in the lattice are essential factors to control the electrical conductivity. It is therefore of great importance to investigate the thermal behavior and eventual residential sites of impurity ions in the ZnO matrix; for that purpose, it is necessary to obtain local information around dilute donor ions with high sensitivity.

For a microscopic investigation of local sites, nuclear spectroscopic techniques are highly suited because detection of high energy radiations from unstable nuclei enables accurate analysis of the local structure at extremely dilute impurities. Time-differential perturbed angular correlation (TDPAC) spectroscopy is a powerful nuclear spectroscopic technique, which can provide atomic level information on the local structures and/or internal fields at the site of the radioactive nuclear probe through hyperfine interactions between the nuclear moment(s) and the surrounding spins and charge distribution [15–17]. By detecting high-energy photons ($10^5$-eV $\gamma$ rays) with excellent time resolution, this spectroscopy fulfills the present requirement for the investigation of specific local sites of dilute impurities. Taking advantage of this spectroscopy, in our previous work, we introduced In impurities in polycrystalline ZnO by means of a simple solid state reaction, and measured the local fields at their residential sites with the $^{111}$In probe [18–21], which disintegrates to the daughter nucleus $^{111}$Cd by an electron capture (EC) decay process. The radioactive probe is expressed as $^{111}$In($\rightarrow^{111}$Cd) hereafter. By the analysis of the TDPAC spectra, we found the following facts on the local structures at the probe: (1) heat treatment in air for thermal diffusion of In ions into ZnO matrix causes their aggregation to form $ZnIn_2O_4$-like nanosized structures as a secondary phase [18], and (2) subsequent heating in vacuum makes the nanoscale cluster decomposed, resulting in the release of In ions into the Zn lattice site by thermal diffusion [21]. The latter phenomenon signifies the successful occupation of lattice positions by the released In ions, which function as donors in ZnO. However, the previous work left a problem to be overcome: thermal diffusion of the In ions followed by the decomposition of the nanosized cluster was observed only for those at low concentration <0.05 at. %, and the decomposition was not completed leaving a significant amount of residual clusters in the ZnO matrix. Because the

*wsato@se.kanazawa-u.ac.jp

 

clusters could be a cause of electrical resistance, their complete decomposition leading to an increase of higher carrier density is highly desired.

The objective of the present work is to establish a method for complete substitution of In dopants for Zn in polycrystalline ZnO at higher concentration by solid state reaction to maximize its conductivity. Thus, we conducted TDPAC measurements with the $^{111}$In($\rightarrow^{111}$Cd) probe to monitor In behavior and investigated the correlation between the concentration of In substitutes and the electrical conductivity from microscopic and macroscopic points of view. Based on the observation of thermal behavior of In impurities and O vacancies varying with the heat-treatment condition, the present paper proposes a strategy for the introduction of 0.5 at. % In donors into defect-free substitutional Zn sites in polycrystalline ZnO.

## II. EXPERIMENT

### A. Preparation of In-containing ZnO

We adopted the following simple solid state reaction to introduce In ions in polycrystalline ZnO. Powder $In(NO_3)_3 \cdot 3H_2O$ of a purity of 99.99% was dissolved in ethanol, and a stoichiometric amount of powder ZnO of a purity of 99.999% was put in the solution for the preparation of 0.5 at. % In-containing ZnO (denominated IZO hereafter). The suspension containing Zn and In was stirred while being heated at about 320 K on a magnetic stirrer. After the mixture was dried up, the powder was then mixed in a mortar to uniformity. The powder was pressed into a disk, and heat treatment was performed in air at 1273 K for 3 h. For the characterization of the synthesized IZO, powder x-ray diffraction (XRD) pattern was obtained using Cu-$K\alpha$ radiation to check for the possible formation of unwanted secondary phases.

### B. TDPAC spectroscopy

For the microscopic examination of the local fields at In sites, we adopted TDPAC spectroscopy in this work as well because of its capability of tracing the thermal behavior of In ions by the $^{111}$In($\rightarrow^{111}$Cd) probe. The experimental procedure is described below and is schematically shown in Fig. 1.

Commercially available $^{111}$In HCl solution was added in droplets onto the disks of IZO prepared above. The total radioactivity was approximately 300 kBq. After drying up the sample disk with a heat lamp, it was again heated in air at 1373 K for 2 h in order to thermally diffuse the radioactive $^{111}$In in the ZnO matrix. A TDPAC measurement was then performed for the heat-treated sample at room temperature (step 1). Subsequently to the step 1 measurement, the sample was sealed in a quartz tube in vacuum, and heated at 1273 K for 2 h. This vacuum heating was for the dissociation of Zn-In nanostructures to release In ions to substitutional Zn sites [21]. After cooling down to room temperature, the sample was resealed in a different quartz tube, and the same heat treatment was repeated again; that is, 4-h vacuum heating was conducted in total for the sample. The significance of the two-step heating is described in Sec. III B. A TDPAC measurement was again performed at room temperature for the vacuum-heated IZO (step 2-1). After the measurement, the IZO sample further underwent a two-step (2 h × 2) heat

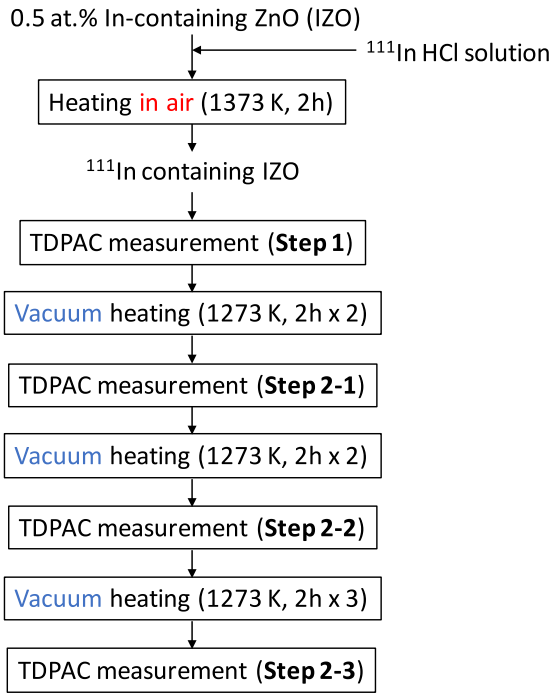


FIG. 1. Experimental procedure of the multistep syntheses of IZO for TDPAC measurements.

treatment by the same procedure above; i.e., 8-h (2 h × 2 + 2 h × 2) vacuum heating was conducted for the IZO. Then, another TDPAC measurement was performed for the sample at room temperature (step 2-2). The vacuum heating was further repeated for the measured IZO sample; this time three-step (2 h × 3) heating was done, meaning that the sample was heated in vacuum for 14 h in total (2 h × 2 + 2 h × 2 + 2 h × 3). Finally, a TDPAC measurement was performed again at room temperature (step 2-3).

All the TDPAC measurements were performed by the detection of the 171–245-keV cascade $\gamma$ rays with the intermediate nuclear spin state of $I = 5/2$ having a half-life of 85.0 ns [22]. We observed the directional anisotropy of the propagation directions of the successive $\gamma$ rays as a function of the time interval of their emissions by operating the delayed coincidence events with the following relation:

$$A_{22}G_{22}(t) \approx \frac{2[N(\pi, t) - N(\pi/2, t)]}{N(\pi, t) + 2N(\pi/2, t)}, \quad (1)$$

where $A_{22}$ denotes the angular correlation coefficient representing the magnitude of the directional anisotropy of the cascade $\gamma$ rays, $G_{22}(t)$ is the time-differential perturbation factor as a function of the time interval $t$ between the cascade $\gamma$-ray emissions, and $N(\theta, t)$ is the number of the delayed coincidence events observed at an angle $\theta$. For the $\gamma$-ray detection, $BaF_2$ scintillation detectors were adopted due to their excellent time resolution.

### C. Electrical conductivity measurements

The experimental procedure for the electrical conductivity measurements of IZO samples is schematized in Fig. 2. The four-point probe system was adopted for the measurements.

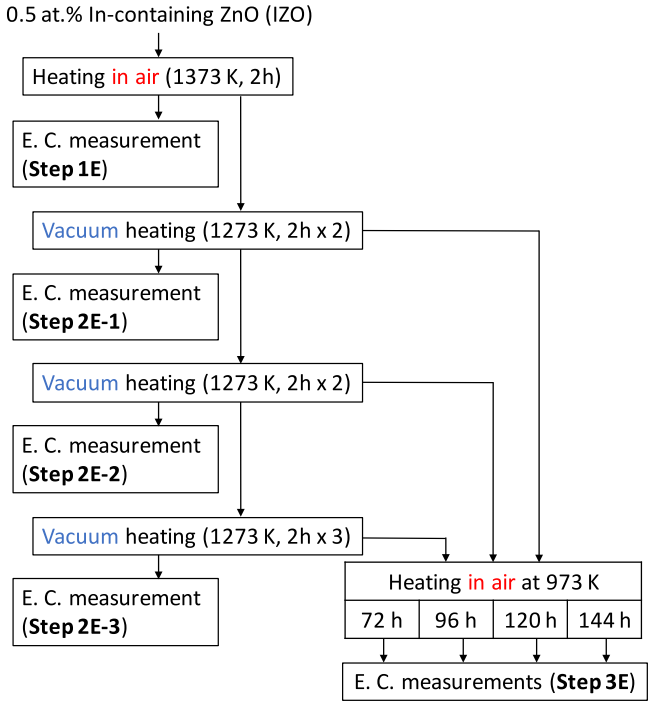


FIG. 2. Experimental procedure of the multistep syntheses of IZO for electrical conductivity (E. C.) measurements.

An IZO sample synthesized by the same procedure described in Sec. II A was heated in air at 1373 K for 2 h; this treatment was for a comparative study with the result of the TDPAC measurement, and it was therefore needed to heat the sample in the same condition as that for the $^{111}$In diffusion before the TDPAC measurement of step 1. Electrical conductivity was measured at room temperature for the sample disk heat-treated above (step 1E).

Subsequently, conductivities were measured at room temperature for three IZO disk samples heat-treated in vacuum by the same procedure as those TDPAC-measured in steps 2-1 to 2-3, respectively, to observe vacuum-heating time dependence of electrical conductivity (steps 2E-1 to 2E-3).

### D. X-ray photoelectron spectroscopy

For the analysis of the chemical states of Zn and O on the surface of undoped ZnO samples heat treated in air and in vacuum, x-ray photoelectron spectroscopy (XPS) measurements were performed with a JEOL JPS-9010 using a standard Mg-$K\alpha$ x-ray radiation source (10 mA, 10 kV). Binding energy correction was carried out with a reference peak of C1$s$. From the spectral analysis, we investigated the effect of high temperature exposure of ZnO samples on different atmospheric conditions.

## III. RESULTS AND DISCUSSION

### A. Structural characterization

Structural characterization of the polycrystalline IZO was carried out based on its powder XRD pattern. The room-temperature diffractogram is shown in Fig. 3 together with that of undoped ZnO for comparison. It was confirmed that the

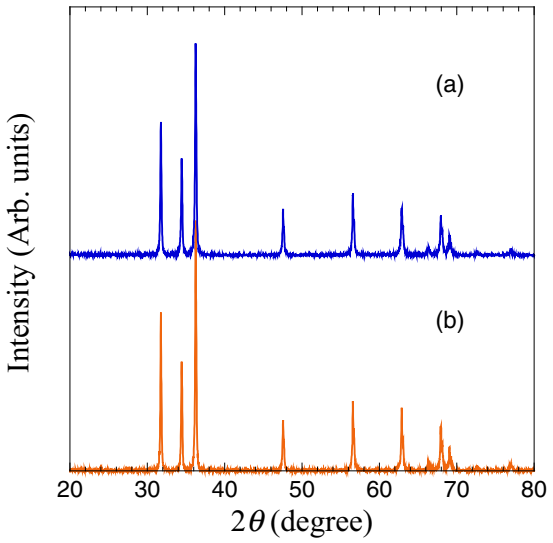


FIG. 3. Powder x-ray diffraction patterns (a) of IZO and (b) of undoped ZnO.

lattice constants remained unchanged with the introduction of 0.5 at. % In and new phases possibly arising from the impurities were not at all detected within the detection precision. As demonstrated in our previous work and mentioned above [20,21], however, nanosized structures formed by In impurities and Zn ions were detected by TDPAC spectroscopy as described below.

### B. Control and detection of In sites: TDPAC studies

The room-temperature TDPAC spectra obtained by the measurements of steps 1 to 2-3 are shown in Fig. 4. Because the present samples as well as the $^{111}$In($\rightarrow^{111}$Cd) probe are nonmagnetic, all the perturbation patterns can be regarded as being of electric quadrupole interactions between the probe nuclei and the electric field gradients (EFGs) produced at the probe nuclei by extranuclear charge distribution. Since IZO may have electrical conductivity between those in an insulator and a semiconductor, the so-called aftereffect should be taken into account for the spectral analyses as proposed in our previous works [18–21]. Thus, we analyzed the spectra with the following time-differential perturbation factor $G_{22}(t)$:

$$G_{22}(t) = G^{*}_{22}(t) G^{\text{static}}_{22}(t). \quad (2)$$

Here, $G^{*}_{22}(t)$ is the time-dependent dynamic perturbation part for the aftereffect operating on the static perturbation factor, $G^{\text{static}}_{22}(t)$ [23–26]. The $G^{*}_{22}(t)$ is expressed as

$$G^{*}_{22}(t) = \frac{\lambda_g}{\lambda_g + \lambda_r} + \frac{\lambda_r}{\lambda_g + \lambda_r} \exp[-(\lambda_g + \lambda_r)t], \quad (3)$$

where $\lambda_g$ is the reciprocal of the recovery time $\tau_g$ to the ground state of the probe atom, and $\lambda_r$ denotes the Abragam and Pound relaxation constant [27]. This effect is typically observed for the probe disintegrating to its daughter by the EC decay such as the present $^{111}$In($\rightarrow^{111}$Cd). (Immediately after the electron capture, rearrangement of the orbital electrons of $^{111}$Cd takes place, which causes damping of the $\gamma$-$\gamma$ anisotropy by dynamic perturbation of the electrons

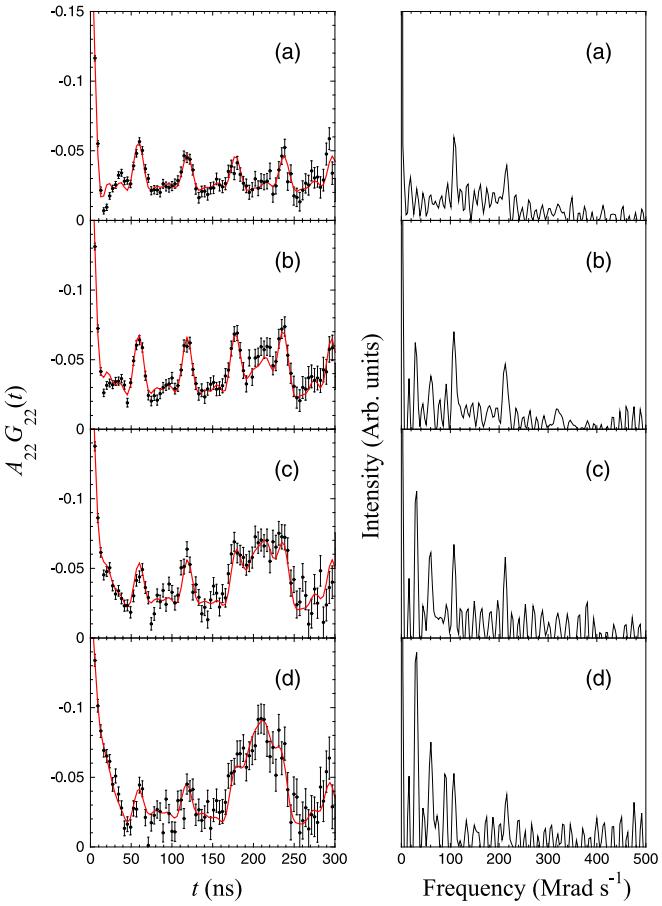


FIG. 4. Room-temperature TDPAC spectra of $^{111}$In($\rightarrow^{111}$Cd) in IZO (left) and their Fourier transformed spectra (right) heat treated (a) at 1373 K for 2 h in air, and at 1273 K (b) for 4 h (2 h × 2), (c) for 8 h (2 h × 4), and (d) for 14 h (2 h × 7) in vacuum after the measurement of (a).

surrounding the nucleus. From the recovery time of the spectral damping, we can obtain information on the behavior of electrons surrounding the nucleus.) For a polycrystalline sample, $G_{22}^{\text{static}}(t)$ in Eq. (2) is explicitly written for $I = 5/2$ as

$$G_{22}^{\text{static}}(t) = \sigma_{2,0} + \sum_{n=1}^{3} \sigma_{2,n} \cos(\omega_n t), \tag{4}$$

where $\sigma_{2,n}$ are functions only of the asymmetry parameter $\eta = (V_{xx}–V_{yy})/V_{zz} (0 \leqslant \eta \leqslant 1)$ for the principal axes of the EFG chosen as $|V_{xx}| \leqslant |V_{yy}| \leqslant |V_{zz}|$, and the frequencies $\omega_n$ are functions of $\eta$ and the electric quadrupole frequency $\omega_Q$ written as

$$\omega_Q = -\frac{eQV_{zz}}{4I(2I-1)\hbar}. \tag{5}$$

In the case that the asymmetry parameter $\eta = 0$, for example, $\omega_n$ are related to $\omega_Q$ in such a way as $\omega_1 = 6\omega_Q$, $\omega_2 = 12\omega_Q$, and $\omega_3 = 18\omega_Q$. In Eq. (5), the quadrupole moment of the probe nucleus at the relevant intermediate state of the cascade is $Q = 0.76(2)$b [22], $e$ is the charge of an electron, and the other symbols have the usual meanings. The hyperfine interaction parameter values obtained by the fit are listed in Table I. With respect to the fraction, it is obvious that there is another component of ∼10% fraction other than the components with oscillatory structures (C1 and C2 described below) in each spectrum. Due to the polycrystalline samples, these components may arise from the probes in various grain boundaries. Because it is almost impossible to differentiate all the small contributions having diverse frequencies, we regarded all the contributions as the third component forming a backgroundlike constant plateau.

The spectrum in Fig. 4(a) is of the $^{111}$In($\rightarrow^{111}$Cd) probe in the IZO heated in air. The oscillatory pattern composed of a single component (C1 hereafter) has reproduced the one obtained in our previous work, demonstrating that the probe is involved in $ZnIn_2O_4$-like nanosized structures [18,20]. Because these structures hinder electrical conduction by electron scattering, a system with no secondary phase should ideally be produced with In ions occupying the lattice positions to function as donors. As previously reported [21], subsequent vacuum heating of the sample makes it possible to dissociate the nanostructures, releasing In ions into substitutional Zn sites by thermal diffusion. It is inferred that this process is triggered by the release of oxygen atoms from the nanostructure in high-temperature vacuum, which induces local charge imbalance in the structure, resulting in the expulsion of In ions from the nanosized aggregates [28]. Thus, the vacuum heating is effective for In ions to occupy substitutional Zn sites. However, this method was valid only for ZnO with In impurities as dilute as 0.01 at. %, and was no longer applicable to those with more concentrated In of 0.05 at. %, for example [21]. We assumed for the limited effect that a sealed quartz

TABLE I. Hyperfine interaction parameter values obtained by the fits to the spectra in Fig. 4.

| Spectrum in Fig. 4 | Component | $\omega_Q$ (Mrad s$^{-1}$) | Fraction (%) | $\lambda_g$[a] ($10^9$ s$^{-1}$) | $\lambda_r$[a] ($10^9$ s$^{-1}$) |
|---|---|---|---|---|---|
| (a) | C1 | 17.5(1) | 89(1) | 0.0055(8) | 0.043(4) |
| (b) | C1 | 17.7(1) | 74(2) | 0.013(3) | 0.049(2) |
| | C2 | 5.0(1) | 13(2) | 0.0711 | 0.0501 |
| (c) | C1 | 17.6(1) | 60(10) | 0.021(1) | 0.08(8) |
| | C2 | 5.0(1) | 29(8) | 0.0711 | 0.0501 |
| (d) | C1 | 17.8(1) | 27(7) | 0.035(15) | 0.04(4) |
| | C2 | 5.0(1) | 61(6) | 0.0711 | 0.0501 |

[a]$\lambda_g$ and $\lambda_r$ values for C2 were fixed with the average values of those obtained in our previous work [18].

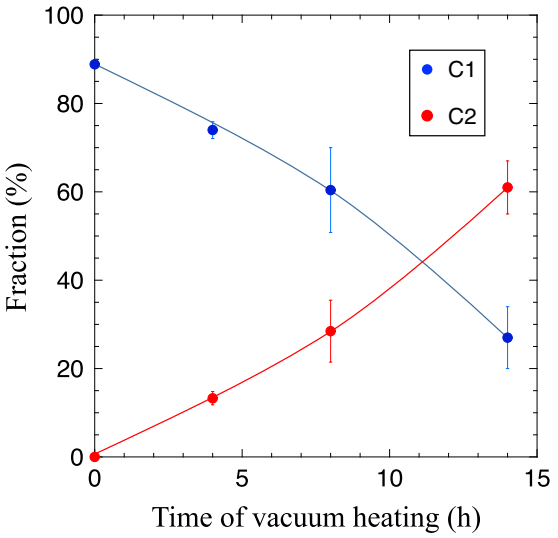


FIG. 5. Vacuum-heating-time dependence of the fractions of C1 (blue) and C2 (red). The solid lines are guides to the eye.

tube under vacuum becomes filled with the decomposed oxygen molecules released from ZnO matrix in the main and the nanostructures, reaching equilibrium with oxygen ions in the sample at a certain vacuum-heating time. Thus, we expected that repeated vacuum heating in renewed quartz tubes would enhance the evacuation of oxygen ions from the nanostructures to release more In ions into substitutional Zn sites as donors.

In order to corroborate the assumption, 2-h heat treatments were repeated by resealing vacuum-heated samples in different quartz tubes every time (see Fig. 1). TDPAC measurements were performed for the sample vacuum heated step by step at steps 2-1 to 2-3, and the corresponding room-temperature spectra are shown in Figs. 4(b)–4(d), respectively. In addition to the single component C1 appearing in Fig. 4(a), another component with a low quadrupole frequency (C2 hereafter) emerged in the spectra in Figs. 4(b)–4(d). As interpreted in previous works [29–33], C2 arises from the $^{111}$In($\rightarrow ^{111}$Cd) probe in defect-free substitutional Zn sites. Vacuum-heating-time dependencies of the fractions of the two components are shown in Fig. 5. The C2 fraction increases and C1 decreases contrarily as the heating time becomes longer. This result signifies that a great fraction of In ions trapped in the nanostructures successfully escaped to Zn substitutional sites, allowing themselves to function as the donor.

### C. Correlation between the concentration of In donors and electrical conductivity

In the next stage, we investigated the correlation between the fraction of In donors (C2) and the electrical conductivity of the samples prepared under the same condition. The conductivity is plotted as a function of vacuum heating time in Fig. 6. The behavior of C2 shown in Fig. 5 is also exhibited for easy comparison. The electrical conductivity reaches the ceiling by 4-h heating; obviously, the conductivity is not correlated with the C2 fraction. (As is explained below, however, we demonstrate a clear correlation between the conductivity

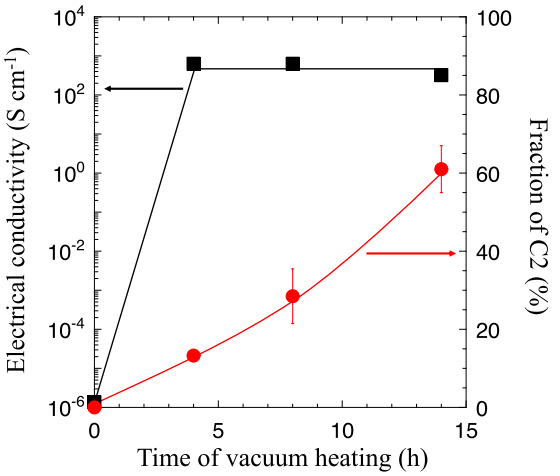


FIG. 6. Vacuum-heating-time dependence of the electrical conductivity of IZO. The fraction of C2 is also shown for comparison.

and the C2 fraction.) Because the saturated conductivity of about $1 \times 10^3$ S cm$^{-1}$ is close to the values generally observed for metals (with some exceptions, e.g., Ti), it is considered that another factor other than the In donor doping should contribute to the high conductivity. We assumed from the observation that oxygen deficient (leading to Zn-rich metallic) layers were formed on the surfaces of the samples by the high-temperature heating in vacuum. This assumption was supported by the result of an additional experiment that the same heat treatments for undoped ZnO led to a similar result as shown in Fig. 7. [Apart from the similar vacuum-heating-time dependence, the following two experimental facts should be noted: (1) the saturated conductivity of IZO shown in Fig. 6 is higher by two orders of magnitude than that of the undoped one shown in Fig. 7, which evidently reflects the effect of In doping as proved by the parameters in Table II obtained by additional Hall effect measurements, and (2) the conductivity of IZO at zero-h vacuum heating ($=1.4 \times 10^{-6}$ S cm$^{-1}$) shown in Fig. 6 is lower than the corresponding value for undoped

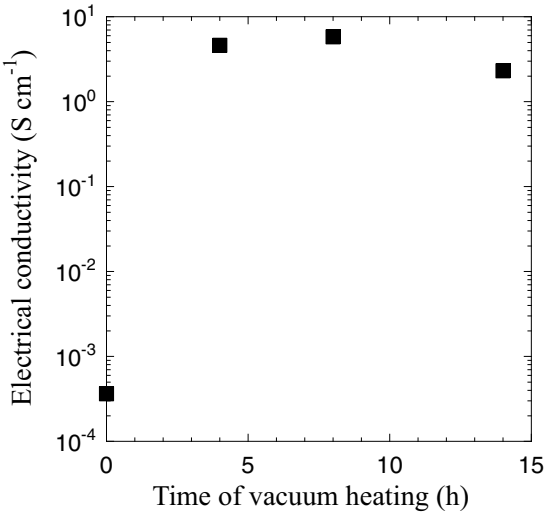


FIG. 7. Vacuum-heating-time dependence of the electrical conductivity of undoped ZnO.

TABLE II. Parameter values obtained by Hall effect measurements for the samples heat treated in vacuum. The sample was synthesized in the same procedure as that for step $2 \times 10^{-1}$.

| Sample | $R_H$ ($cm^3\,C^{-1}$)[a] | $n$ ($cm^{-3}$)[b] | $\mu$ ($cm^2\,V^{-1}\,s^{-1}$)[c] | $\sigma$ ($S\,cm^{-1}$)[d] |
|---|---|---|---|---|
| Undoped | $-31$ | $2.0 \times 10^{17}$ | $1.0 \times 10^2$ | 3.2 |
| In-doped | $-3.1 \times 10^{-2}$ | $2.0 \times 10^{20}$ | 15 | $4.8 \times 10^2$ |

[a]Hall coefficient.
[b]Carrier concentration.
[c]Mobility.
[d]Electrical conductivity.

ZnO ($=3.6 \times 10^{-4}\,S\,cm^{-1}$) shown in Fig. 7, which signifies conduction electron scattering by the nanosized structures formed in IZO.]

In order to verify the above assumption on the formation of oxygen-deficient surfaces, we carried out XPS measurements to examine the chemical states of Zn and O on the surfaces of undoped ZnO samples prepared by the same procedure as those for the electrical conductivity measurements at steps 1E and 2E-1. Figure 8 shows their XPS spectra at the binding energy regions of O1$s$, Zn2$p_{3/2}$, and Zn2$p_{1/2}$ peaks. For the O1$s$ peaks, one can see two components for both samples heated in air and in vacuum. The lower binding-energy components indicated with a blue line can be assigned to intrinsic $O^{2-}$ ions at defect-free lattice sites in ZnO with the wurtzite structure, whereas for the green line components at higher binding energy, they are generally attributed to $O^{2-}$ ions residing in oxygen deficient regions [13,34,35]. Obviously, the high energy component is enhanced in the vacuum heated sample compared to that for the one heated in air. As regards the Zn2$p_{3/2}$ and Zn2$p_{1/2}$ peaks, the sample heated in air exhibits single peaks assignable to $Zn^{2+}$ ions in the wurtzite ZnO. For the vacuum heated sample, however, small components emerge in both of the 2$p_{3/2}$ and 2$p_{1/2}$ peaks at the high energy region. Taking into account that the 2$p$ peaks originating from Zn(0) are generally observed at the higher energy region [36], these small peaks can be assigned to metallic Zn formed in the vacuum heated ZnO. These results of the XPS analysis are consistent with the metal-like electrical conductivity observed for the vacuum heated samples.

As another effect on the enhancement of the conductivity, a change of the grain size before and after the vacuum heating can be pointed out because the conduction electrons are likely to be scattered at grain boundaries. In order to check the possible effect, scanning electron micrographs were obtained for undoped ZnO as shown in Fig. 9. Both samples with and without vacuum heat treatment have almost the same grain sizes of about several micrometers. This observation demonstrates that the key effect on the conductivity is not the grain size of ZnO.

The observations of the electrical conductivity and XPS experiments evidently suggest that after the vacuum heating the composition of IZO is not homogeneous due to the emergence of a metallic phase on the surface, and thus the samples are not real semiconductors as they are. In order to regenerate the stoichiometric ZnO phase on the surface by filling the oxygen vacancies with oxygen atoms, therefore,

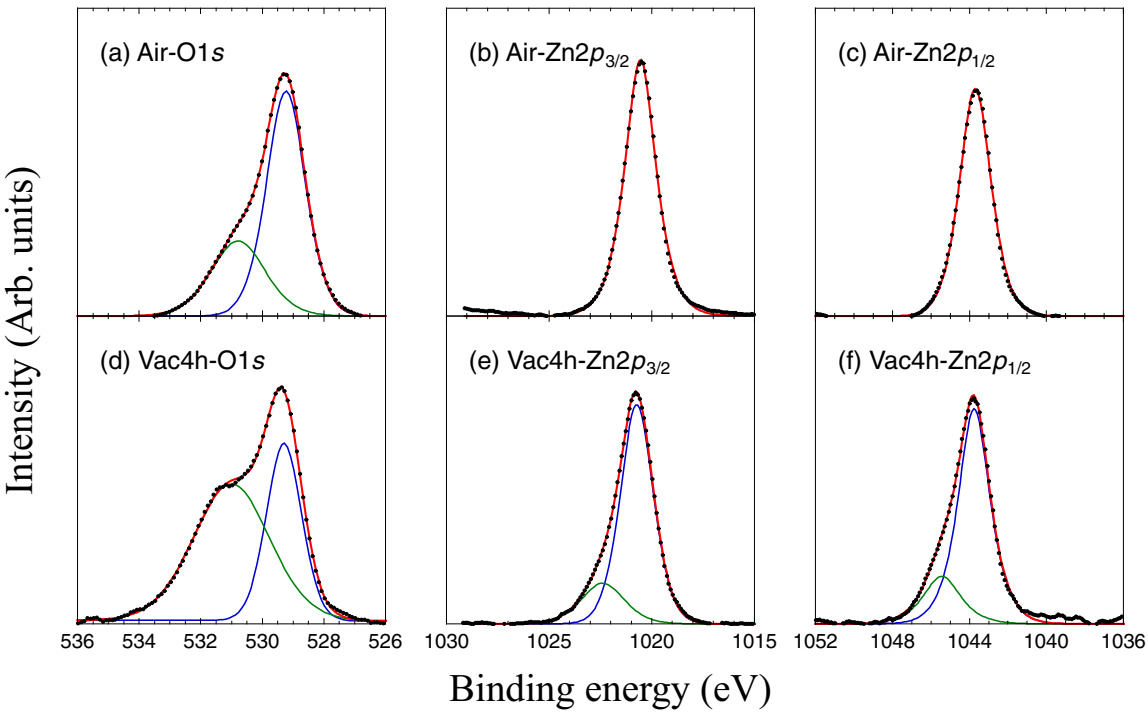


FIG. 8. X-ray photoelectron spectra of undoped ZnO at the binding energy regions of O1$s$, Zn2$p_{3/2}$, and Zn2$p_{1/2}$ peaks. The samples were heat treated in Air at 1373 K [indicated as Air in the spectra of (a), (b), and (c)] and subsequently heated for 4 h (2 h × 2) in vacuum at 1273 K [indicated as Vac4h in (d), (e), and (f)]. The observed data are shown with the dotted lines, and the results of fits are the solid lines; the red lines are the total and blue and green lines represent subcomponents.

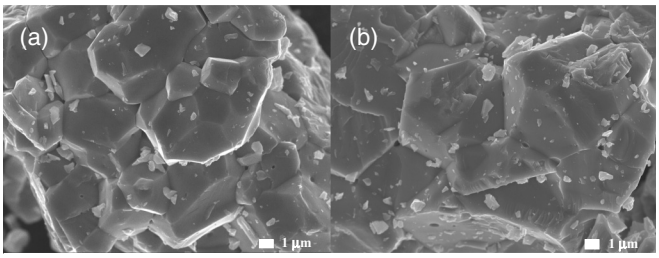


FIG. 9. Scanning electron micrographs of undoped ZnO (a) heated for 2 h in air at 1373 K and (b) subsequently heated for 4 h (2 h × 2) in vacuum at 1273 K.

the samples with metallic surfaces underwent step-by-step heat treatments in air at 973 K for 72, 96, 120, and 144 h, and every heating was followed by an electrical conductivity measurement at room temperature (see Fig. 2 for the procedure) [37]. Figure 10 exhibits the heat-treatment time dependence of electrical conductivity of the samples. The conductivities decreased as the heating time becomes long, but they ended up respective constant values depending on each preceding heat-treatment time in vacuum. Regarding the constant values as the eventual electrical conductivities, they are plotted as functions of vacuum-heating time and of the C2 fraction in Figs. 11(a) and 11(b), respectively. One can see clear correlations between the conductivity and the parameters on the abscissa, signifying that the heat treatment of IZO in vacuum has made progress with dissociation of the $ZnIn_2O_4$-like nanostructured precipitates. From these observations, it was found that electrical conductivity observed for 0.5 at. % In-doped ZnO ($2.5 \times 10^1$ S cm$^{-1}$) was raised as high as five orders of magnitude compared with undoped ZnO without vacuum heating ($=3.6 \times 10^{-4}$ S cm$^{-1}$) (see Fig. 7).

The present atomic-level observation evidently demonstrates that substitution of In ions in defect-free Zn sites

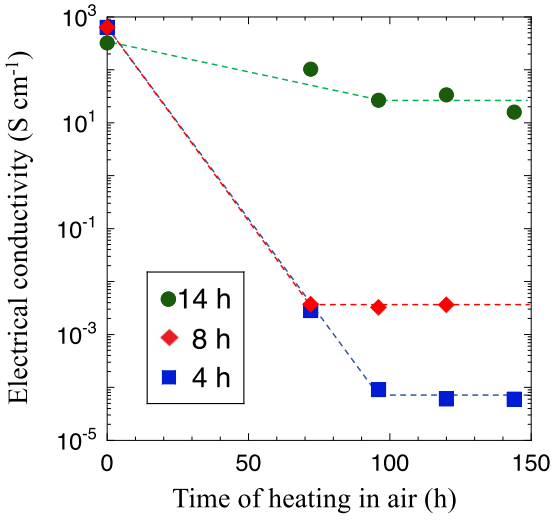


FIG. 10. Dependence of the electrical conductivity of IZO on time of heating at 973 K in air. Each sample was pretreated by vacuum heating at 1273 K for the duration indicated. The dashed lines are guides to the eye.

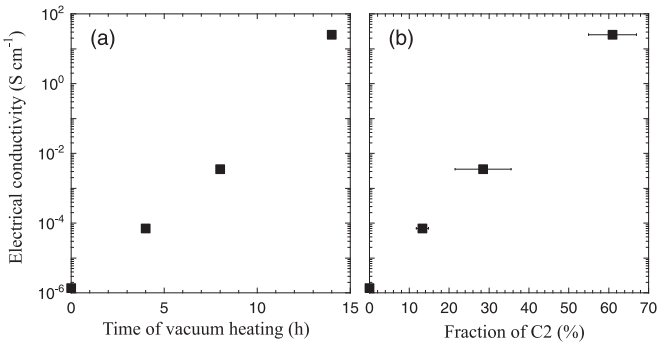


FIG. 11. (a) Vacuum-heating time and (b) C2 fraction dependences of the electrical conductivity of IZO. The values of each conductivity are the averages of the constant values observed by heat treatment in air shown in Fig. 10.

indeed gives birth to conduction electrons. The next interest is to apply the present method to more heavily doped ZnO to realize much higher conductivity. As regards Al and Ga, other candidates for donors in ZnO, they have already exhibited excellent conductivity with heavier doping (3.0 and 5.7 wt %, respectively) [38]. We also expect that the application of the present donor-introduction method can further enhance the electrical conductivities of Al- and Ga-doped ZnO as well.

## IV. SUMMARY AND CONCLUSIONS

In the present work, we tried to control association-dissociation behavior of In impurities introduced in polycrystalline ZnO by monitoring their thermal behavior by means of time-differential perturbed angular correlation spectroscopy. A multistep doping method was applied to 0.5 at. % In-containing ZnO, in which the sample underwent combined heat treatments in air and in vacuum, and we have successfully introduced a great fraction of In dopants into defect-free substitutional Zn sites by the method. However, it was found that the concentration of the In dopants does not correlate with the electrical conductivity. In order to investigate the cause, we performed an XPS experiment and revealed that the surface of the sample became metallic as a result of the formation of oxygen-deficient layers due to vacuum heating. For the purpose of refilling the O vacancies on the surface with O atoms, the samples were heat treated in air again. We succeeded in observing a clear correlation between the electrical conductivity and the concentration of In donors, and eventually achieved electrical conductivity as high as five orders of magnitude compared with undoped ZnO. The present work has established a controlling method of In sites in ZnO. The next interest is to apply the present method to more heavily doped ZnO to realize much higher conductivity.

## ACKNOWLEDGMENTS

The authors are grateful to Dr. H. Sugiyama and Dr. S. Ochiai of Kanazawa University for their technical cooperation in the XPS experiment and the particle size measurement. The present work was supported in part by JSPS KAKENHI Grant No. 26286075, No. 18H03692, and No. 22K12661.

[1] Y. Mei, S. Pandey, W. Long, J. Liu, S. Zhong, L. Zhang, S. Du, and D. Xu, Processing and characterizations of flash sintered ZnO-$Bi_2O_3$-$MnO_2$ varistor ceramics under different electric fields, J. Eur. Ceram. Soc. **40**, 1330 (2020).

[2] W. Liu, L. Zhang, F. Kong, K. Wu, S. Li, and J. Li, Enhanced voltage gradient and energy absorption capability in ZnO varistor ceramics by using nano-sized ZnO powders, J. Alloys Compd. **828**, 154252 (2020).

[3] M. M. Obeid, H. R. Jappor, K. Al-Marzoki, I. A. Al-Hydary, S. J. Edrees, and M. M. Shukur, Unraveling the effect of gd doping on the structural, optical, and magnetic properties of ZnO based diluted magnetic semiconductor nanorods, RSC Adv. **9**, 33207 (2019).

[4] A. K. Rana, Y. Kumar, P. Rajput, S. N. Jha, D. Bhattacharyya, and P. M. Shirage, Search for origin of room temperature ferromagnetism properties in Ni-doped ZnO nanostructure, ACS Appl. Mater. Interfaces **9**, 7691 (2017).

[5] A. Samanta, M. N. Goswami, and P. K. Mahapatra, Magnetic and electric properties of Ni-doped ZnO nanoparticles exhibit diluted magnetic semiconductor in nature, J. Alloys Compd. **730**, 399 (2018).

[6] T. Dietl, H. Ohno, F. Matsukura, J. Cibert, and D. Ferrand, Zener model description of ferromagnetism in zinc-blende magnetic semiconductors, Science **287**, 1019 (2000).

[7] H. -Y. Liu, V. Avrutin, N. Izyumskaya, U. Ozgur, and H. Morkoc, Transparent conducting oxides for electrode applications in light emitting and absorbing devices, Superlattices Microstruct. **48**, 458 (2010).

[8] D. Zhao, S. Sathasivam, J. Li, and C. J. Carmalt, Transparent and conductive molybdenum-doped ZnO thin films via chemical vapor deposition, ACS Appl. Electron. Mater. **2**, 120 (2020).

[9] M. Shekofteh-Gohari, A. Habibi-Yangjeh, M. Abitorabi, and A. Rouhi, Magnetically separable nanocomposites based on ZnO and their applications in photocatalytic processes: a review, Crit. Rev. Environ. Sci. Technol. **48**, 806 (2018).

[10] N. Tripathy, R. Ahmad, H. Kuk, D. H. Lee, Y.-B. Hahn, and G. Khang, Rapid methyl orange degradation using porous ZnO spheres photocatalyst, J. Photochem. Photobiol., B **161**, 312 (2016).

[11] M. Golmohammadi, M. Honarmand, and S. Ghanbari, A green approach to synthesis of ZnO nanoparticles using jujube fruit extract and their application in photocatalytic degradation of organic dyes, Spectrochim. Acta A **229**, 117961 (2020).

[12] D. P. Howard, P. Marchand, I. D. Johnson, C. J. Carmalt, I. P. Parkin, and J. A. Darr, Conducting al and Ga-doped zinc oxides; rapid optimisation and scale-up, J. Mater. Chem. A **4**, 12774 (2016).

[13] D. S. Y. Jayathilake, T. A. N. Peiris, J. S. Sagu, D. B. Potter, K. G. U. Wijayantha, C. J. Carmalt, and D. J. Southee, Microwave-assisted synthesis and processing of Al-doped, Ga-doped, and Al, Ga codoped ZnO for the pursuit of optimal conductivity for transparent conducting film fabrication, ACS Sustainable Chem. Eng. **5**, 4820 (2017).

[14] N. Saxena, R. Sharma, A. Hussain, R. J. Choudhary, A. K. Debnath, O. P. Sinha, and R. Krishna, Effect of the triple (Al, Ga, In) doping in ZnO nanostructures on its transmission, conductivity, and stability for TCO applications, Mater. Lett. **306**, 130886 (2022).

[15] H. Frauenfelder and R. M. Steffen, in *α-, β-, and γ -Ray Spectroscopy*, edited by K. Siegbahn (North-Holland, Amsterdam, 1965), Vol. 2, pp. 997–1198.

[16] G. Schatz and A. Weidinger, *Nuclear Condensed Matter Physics* (Wiley, New York, 1996).

[17] G. Marschick, J. Schell, B. Stöger, J. N. Gonçalves, M. O. Karabasov, D. Zyabkin, A. Welker, M. Escobar C., D. Gärtner, I. Efe, R. A. Santos, J. E. M. Laulainen, and D. C. Lupascu, Multiferroic bismuth ferrite: perturbed angular correlation studies on its ferroic $\alpha$-$\beta$ phase transition, Phys. Rev. B **102**, 224110 (2020).

[18] W. Sato, Y. Itsuki, S. Morimoto, H. Susuki, S. Nasu, A. Shinohara, and Y. Ohkubo, Local fields and conduction-electron behavior at impurity sites in indium-doped ZnO, Phys. Rev. B **78**, 045319 (2008).

[19] W. Sato, S. Komatsuda, and Y. Ohkubo, Characteristic local association of in impurities dispersed in ZnO, Phys. Rev. B **86**, 235209 (2012).

[20] W. Sato, S. Komatsuda, Y. Yamada, and Y. Ohkubo, Detection of spinel $ZnIn_2O_4$ formed as nanostructures in ZnO, Phys. Rev. B **90**, 235204 (2014).

[21] W. Sato, H. Shimizu, S. Komatsuda, and Y. Ohkubo, Thermal behavior of in impurities in ZnO, J. Appl. Phys. **124**, 105101 (2018).

[22] L. Errico, K. Lejaeghere, J. Runco, S. N. Mishra, M. Rentería, and S. Cottenier, Precision of electric-field gradient predictions by density functional theory and implications for the nuclear quadrupole moment and its error bar of the $^{111}$Cd 245 keV $5/2^+$ level, J. Phys. Chem. C **120**, 23111 (2016).

[23] A. G. Bibiloni, J. Desimoni, C. P. Massolo, L. Mendoza-Zelis, A. F. Pasquevich, F. H. Sanchez, and A. Lopez-Garcia, Temperature dependence of electron-capture aftereffects in the semiconductor $In_2O_3$, Phys. Rev. B **29**, 1109 (1984).

[24] A. G. Bibiloni, C. P. Massolo, J. Desimoni, L. A. Mendoza-Zelis, F. H. Sanchez, A. F. Pasquevich, L. Damonte, and A. R. Lopez-Garcia, Time-differential perturbed-angular-correlation study of pure and Sn-doped $In_2O_3$ semiconductors, Phys. Rev. B **32**, 2393 (1985).

[25] U. Bäverstam, R. Othaz, N. de Sousa, and B. Ringström, Aftereffects in the decay of $^{75}$As and $^{197m}$Hg, Nucl. Phys. A **186**, 500 (1972).

[26] G. N. Darriba, E. L. Muñoz, A. W. Carbonari, and M. Rentería, Experimental TDPAC and theoretical DFT study of structural, electronic, and hyperfine properties in ($^{111}$In→)$^{111}$Cd-doped $SnO_2$ semiconductor: ab initio modeling of the electron-capture-decay after-effects phenomenon, J. Phys. Chem. C **122**, 17423 (2018).

[27] A. Abragam and R. V. Pound, Influence of electric and magnetic fields on angular correlations, Phys. Rev. **92**, 943 (1953).

[28] S. Komatsuda, W. Sato, and Y. Ohkubo, Formation energy of oxygen vacancies in ZnO determined by investigating thermal behavior of Al and In impurities, J. Appl. Phys. **116**, 183502 (2014).

[29] Th. Agne, Z. Guan, X. M. Li, H. Wolf, and Th. Wichert, H. Natter, and R. Hempelmann, Doping of the nanocrystalline semiconductor zinc oxide with the donor indium, Appl. Phys. Lett. **83**, 1204 (2003).

[30] S. Deubler, J. Meier, R. Schütz, and W. Witthuhn, PAC studies on impurities in ZnO, Nucl. Instrum. Methods Phys. Res. B **63**, 223 (1992).

[31] H. Wolf, S. Deubler, D. Forkel, H. Foettinger, M. Iwatschenko-Borho, F. Meyer, M. Renn, W. Witthuhn, and R. Helbig, Acceptors and donors in the wide-gap semiconductors ZnO and $SnO_2$, Mater. Sci. Forum **10–12**, 863 (1986).

[32] E. L. Muñoz, M. E. Mercurio, M. R. Cordeiro, L. F. D. Pereira, A. W. Carbonari, and M. Rentería, Dynamic hyperfine interactions in $^{111}$In ($^{111}$Cd)-doped ZnO semiconductor: PAC results supported by ab initio calculations, Phys. B (Amsterdam, Neth.) **407**, 3121 (2012).

[33] Y. Abreu, C. M. Cruz, P. V. Espen, C. Pérez, I. Piñera, A. Leyva, and A. E. Cabal, Electric field gradient calculations in ZnO samples implanted with $^{111}$In ($^{111}$Cd), Solid State Commun. **152**, 399 (2012).

[34] J. C. C. Fan and J. B. Goodenough, X-ray photoemission spectroscopy studies of Sn-doped indium oxide films, J. Appl. Phys. **48**, 3524 (1977).

[35] M. Chen, X. Wang, Y. H. Yu, Z. L. Pei, X. D. Bai, C. Sun, R. F. Huang, and L. S. Wen, X-ray photoemission spectroscopy and auger electron spectroscopy studies of Al-doped ZnO films, Appl. Surf. Sci. **158**, 134 (2000).

[36] M. C. Biesingera, L. W. M. Laua, A. R. Gersonb, and R. St. C. Smart, Resolving surface chemical states in XPS analysis of first row transition metals, oxides and hydroxides: Sc, Ti, V, Cu and Zn, Appl. Surf. Sci. **257**, 887 (2010).

[37] The heat treatment temperature in air was set at 973 K because it was found in another PAC experiment that the $ZnIn_2O_4$-like nanostructures arise again by heat treatments at higher temperature.

[38] J. Jia, A. Yoshimura, Y. Kagoya, N. Oka, and Y. Shigesato, Transparent conductive al and ga doped ZnO films deposited using off-axis sputtering, Thin Solid Films **559**, 69 (2014).